

Particle-in-cell Simulations of the Whistler Heat-flux Instability in Solar Wind Conditions

Abstract

In collision-poor plasmas from space, e.g., solar wind or stellar outflows, the heat flux carried by the strahl or beaming electrons is expected to be regulated by the self-generated instabilities. Recently, simultaneous field and particle observations have indeed revealed enhanced whistler-like fluctuations in the presence of counter-beaming populations of electrons, connecting these fluctuations to the whistler heat-flux instability (WHFI). This instability is predicted only for limited conditions of electron beam-plasmas, and has not yet been captured in numerical simulations. In this Letter we report the first simulations of WHFI in particle-in-cell setups, realistic for the solar wind conditions, and without temperature gradients or anisotropies to trigger the instability in the initiation phase. The velocity distributions have a complex reaction to the enhanced whistler fluctuations conditioning the instability saturation by a decrease of the relative drifts combined with induced (effective) temperature anisotropies (heating the core electrons and pitch-angle and energy scattering the strahl). These results are in good agreement with a recent quasilinear approach, and support therefore a largely accepted belief that WHFI saturates at moderate amplitudes. In the anti-sunward direction the strahl becomes skewed with a pitch-angle distribution decreasing in width as electron energy increases, which seems to be characteristic of self-generated whistlers and not to small-scale turbulence.

Key words: methods: numerical - plasmas - solar wind - waves - instabilities - interplanetary medium

1. Motivations

Among the kinetic instabilities invoked in the self-regulation of solar wind properties the heat-flux instabilities, and in particular the whistler heat-flux instability (WHFI), are still the most controversial, though in the last decade an increased effort has been devoted to understanding their fundamental properties (Saito & Gary 2007a; Pavan et al. 2013; Seough et al. 2015; Saeed et al. 2017a, 2017b; Shaaban et al. 2018a, 2018b, 2019; Lee et al. 2019) and find their signatures in observation (Breneman et al. 2010; Gurgiolo et al. 2012; Wilson et al. 2013; Lacombe et al. 2014; Landi et al. 2014; Stansby et al. 2016; Tong et al. 2019b, 2019a). The WHFI is triggered by the relative drift, $U = |U_c| + U_b$, of the counter-beaming electrons, a central population (summing up the core and halo electrons) here called generically "core" and denoted by the subscript c, and the beam or strahl population (with subscript b) satisfying the zero net-current condition $n_c|U_c| = n_b U_b$; see Gary (1985) and references therein. However, conditions for the whistlers to be excited (resonantly) by the beaming electrons are very restrained, namely, to a beaming velocity limited between two threshold values roughly given by $\theta_c < U_b < \theta_b$, where $\theta_{c,b}$ are thermal velocities (Gary 1985; Shaaban et al. 2018a, 2018b).

pdfelement
The Trial Version

are expected in this case only for low v the lower threshold (Gary et al. 1999b;) that seems to be confirmed by the al. 1999a, 1999b; Tong et al. 2018). s may also satisfy resonance conditions

with both electron populations, especially for more energetic beams $(U_b > \theta_b)$, but never develop because they are competing with the other faster-growing modes, e.g., the electrostatic

beam-plasma instabilities or the oblique instabilities (Gary & Saito 2007; Saito & Gary 2007a; Seough et al. 2015; Saeed et al. 2017a; Horaites et al. 2018; Lee et al. 2019; Vasko et al. 2019; Verscharen et al. 2019a). If the core electrons exhibit an important temperature anisotropy $T_{c,\perp} > T_{c,\parallel}$ the regime of WHFI may be significantly altered, becoming specific to a standard whistler instability driven by temperature anisotropy, with lower thresholds and higher growth rates (Seough et al. 2015; Shaaban et al. 2018b).

The first investigations of WHFI have been stimulated by observations suggesting a potential implication of whistlers in the regulation of suprathermal populations. If binary collisions are rare, in the solar wind the electron heat flux is less than a conventional Spitzer-Härm level (Spitzer & Härm 1953), and such constraint is attributed mainly to the wave-particle interactions (Bale et al. 2013). Moreover, with the expansion of the solar wind the electron halo shows a continuous build-up on the expense of strahl that lowers in intensity and undergoes a pitch-angle scattering (Maksimovic et al. 2005; Pagel et al. 2007; Gurgiolo et al. 2012; Berčič et al. 2019). In the absence of collisions an immediate explanation for these evolutions is offered by the small-scale wave turbulence and/or the fluctuations self-generated by the instabilities. Higher plasma beta conditions stimulate the implication of self-generated instabilities in the regulation of suprathermal populations, in particular of the electron strahls (Pilipp et al. 1987; Crooker et al. 2003).

Theory and simulations have confirmed that whistler fluctuations, either predefined by a power spectrum decreasing monotonically with increasing frequency or self-generated by kinetic instabilities, can pitch-angle and energy scatter the suprathermal electrons and lead to asymmetric beaming-like distributions, broader (bulge) or decreasing (skewness) in pitch angle at larger electron energies (Vocks & Mann 2003; Vocks et al. 2005; Saito & Gary 2007a, 2007b; Seough et al. 2015). In particular, for the WHFI quasilinear (QL) studies have also suggested a potential role in the limitation of the electron heat flux, probably by the same mechanisms, which reduce the relative drift and induce effective anisotropies of electron populations (Gary & Feldman 1977; Shaaban et al. 2019). However, a confirmation of these effects in simulations has yet to be reported. To our knowledge, numerical experiments have provided extended descriptions only for other branches of heatflux instabilities, e.g., electrostatic beam-plasma, firehose-like (Gary & Saito 2007; Lee et al. 2019), or for the temperature anisotropy-driven instabilities (Saito & Gary 2007a; Seough et al. 2015).

Limiting conditions predicted for the WHFI (Gary 1985; Shaaban et al. 2018a) and small amplitudes of the resulting fluctuations (Shaaban et al. 2019; Tong et al. 2019a) might have also prevented a direct detection in the observations, and sometimes led to contradictory correlations between plasma states and fluctuations (Scime et al. 2001). Clear evidences of WHFI in the solar wind have recently been provided by simultaneous electron and field measurements with a well-established connection to the electron counter-beaming populations and their temperature anisotropy (Tong et al. 2019a, 2019b). These observations confirm recent predictions that WHFI must be quenched by a slight anisotropy T_b , T_b , of the beam, but growth rates may significantly be increased by an opposite anisotropy of the core T_c , (Shaaban et al. 2018b).

This Letter reports the first particle-in-cell (PIC) simulations of the WHFI, realistic for solar-wind conditions. The characteristics of this instability (see above) impose serious limitations to describe it using simulations (with realistic parameters), requiring an immense amount of numerical resources, which are practically impossibles with standard approaches. Here we make use of an implicit PIC code developed by Markidis et al. (2010), which is able to resolve multiple temporal and spatial scales that are characteristic to the solar-wind plasma dynamics (Verscharen et al. 2019b) without the strict limitations in time step and grid spacing imposed typically in explicit codes. Simulations capture the energy transfer between the electron core and beam populations, and correctly describe the saturation of WHFI via the relaxation of the velocity distributions. A QL approach allows time variations of the moments of the distribution (e.g., drifts, temperatures), but implies only a single-wave mode in the energy and momentum transfers (Shaaban et al. 2019). Instead, the simulations enable QL and nonlinear effects of multiple (concurrent, coupled) wave modes.

2. PIC Simulations

Our initial setup in Table 1 is intended for the solar-wind plasma conditions (Maksimovic et al. 2005; Tong et al. 2018, 2011), and for simplicity, both counter-beaming electron

e fixed to protons)

The Trial Version

$$\frac{n_c}{n_e} f_c(\mathbf{w}, \mathbf{v}) + \frac{n_b}{n_e} f_b(\mathbf{w}, \mathbf{v}) \tag{1}$$

are assumed to be Maxwellian distributed. Here n_c and n_b are the core and beam number densities, respectively, and $n_e \equiv n_0$ is the

Table 1
Initial Plasma Parameters for the Simulation

Parameter	Beam (b)	Core (c)	Protons (p)
$\overline{n_j/n_0}$	0.05	0.95	1.0
$T_{j,\parallel}/T_{c,\parallel}$	6.0	1.0	1.0
$eta_{j,\parallel}$	18.0	3.0	3.0
m_p/m_j	1836	1836	1.0
$T_{j,\perp}/T_{j,\parallel}$	1.0	1.0	1.0
U_j/v_A	40.0	-2.1	0.0

total number density of electrons, in a neutral plasma with zero charge $n_e \approx n_i$ and zero net current $n_c U_c + n_b U_b = 0$, where $U_{b,c}$ are the corresponding drift velocities, and here the ions (subscript i) are assumed to be only protons.

We use an implicit one-dimensional PIC code, i.e., iPic3D (Markidis et al. 2010) with a high enough resolution to resolve the electron inertial length and the electron gyromotion. The spatial grid is composed of $n_x = 1024$ cells, with 5000 particles per species per grid. The box size is $L_x =$ 16 d_i , then the cell size is $\Delta x = 0.0156 d_i$. Here $d_i = c/\omega_{pi}$ is the ion inertial length, with $\omega_{pi} = (4\pi \ n_0 e^2/m_p)^{1/2}$ the ion plasma frequency. The mass ratio is $m_p/m_e = 1836$, and the plasma to gyro frequency ratio for ions is $\omega_{pi}/\Omega_{ci}=4390.07$, which implies that the Alfvén speed is $v_A = B_0 / \sqrt{4pn_p m_p} =$ 0.00023c and the plasma to gyro frequency of the electrons is $\omega_{pe}/\Omega_{ce} = 102.48$, which are typical values encountered in solar-wind conditions. The background magnetic field is set in the x direction, $\mathbf{B}_0 = B_0 \hat{\mathbf{x}}$. The time step is $\Delta t = 0.0375/\omega_{pi}$ and the simulations ran until $t_{\text{max}} = 17560.265/\omega_{pi}$ or equivalently $t_{\text{max}} = 4.0/\Omega_{ci}$. In terms of electron quantities, the time step used correspond to $\Delta t = 0.016/\Omega_{ce}$ and the cell size is $\Delta x = 0.7 d_e$.

Figure 1 shows (normalized) time variations, with the increase and saturation of the magnetic power $(W_B = \grave{\mathsf{o}} \mathsf{d} B^2/B_0^2 \, dx)$ of the enhanced fluctuations, as well as the relaxation of the main moments of electron velocity distributions that continue after the instability saturation. The rapid growth of W_B corresponding to the excitation of WHFI in the early stage of the simulations slows down close to $\Omega_i t \approx 3$, and then shows a slower increase up to the end of the simulation, $\Omega_p t = 4.0$. The entire period of the simulation can be identified in this case as characteristic to a pure WHFI. In order to identify this interval of pure whistler-like fluctuations we have used the fast Fourier transforms in space of the transverse magnetic fluctuations ($[FFT(B_y - iB_z)]^2$), which are displayed in Figure 2. In this interval only the intense power of the WHFI corresponding to positive wave numbers are present; see also Figure 3.

Plasma beta parameters $\beta_{c,b} \equiv 8\pi n_0 T_{c,b}/B_0^2$ plotted in Figure 1 are defined with total number density n_0 and reflect therefore the variations of the corresponding temperatures $T_{c,b}$, in parallel (red) and perpendicular (blue) directions with respect to the background magnetic field. Initially isotropic, i.e., $b_{c,}(0) = b_{c,\uparrow}(0)$, the core temperatures are subjected to parallel cooling (red) and small perpendicular heating (blue) by a resonant cyclotron interaction of whistlers with the cooler electrons from the core. Beaming electrons also have isotropic temperatures at the beginning, i.e., $\beta_{b,\parallel}(0) = \beta_{b,\perp}(0)$, but their pitch-angle and energy scattering induces an opposite anisotropy. Consequently, at saturation the core exhibits an excess of perpendicular temperature, i.e., $b_{c,\uparrow}(t^*) > b_{c,\downarrow}(t^*)$, while the

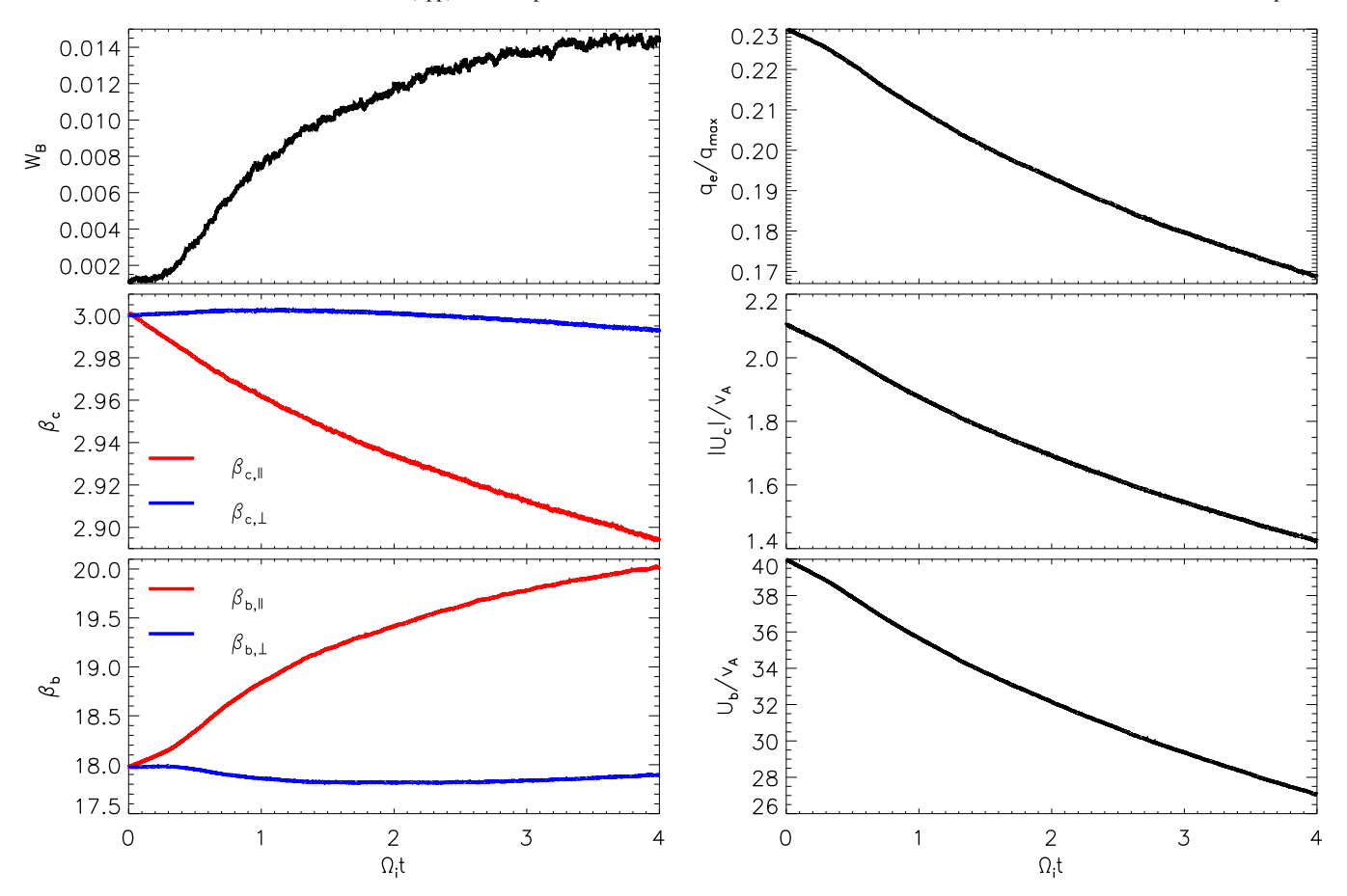


Figure 1. Temporal evolution for the fluctuating magnetic energy density W_B , parallel and perpendicular components of plasma beta parameters $\beta_{c,b}$, normalized (parallel) electron heat flux, and parallel drifts $U_{c,b}$.

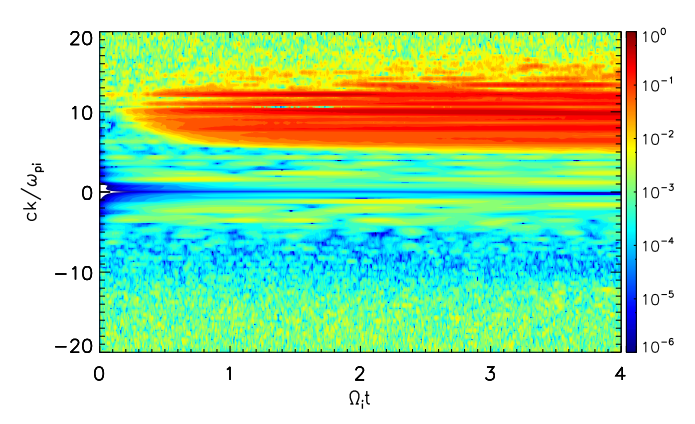


Figure 2. Temporal evolution of the wavenumber transverse magnetic power.

beam shows an excess of parallel temperature, i.e., $b_{b,^{\wedge}}(t^*) < b_{b,^{\wedge}}(t^*)$. Both the linear theory of WHFI (Shaaban et al. 2018b) and the observations (Tong et al. 2019b) indeed suggest that this instability is inhibited by such a temperature anisotropy of the beam. These results are also in good

anisotropy of the beam. These results are also in good a qualitative level and for the same evolutions predicted by theory; see, for ddle panels) and Figure 10 in Shaaban, for such a comparison we have to keep ditions, like the number of particles used

fluctuations in the QL theory, or both, are crucial for the onset time of the instability (López & Yoon 2018).

The right panels in Figure 1 show the time relaxation of the electron heat flux $q_e = m_e/2 \grave{o} dv \ v_x v f_e$ (normalized by $q_{\rm max} = 3n_0 T_c a_c$, $/\sqrt{2}$, where a_c , $= \sqrt{k_B T_c/m_e}$ is the thermal speed), and the core and beam (normalized) drift velocities $(U_{c,b}/v_A)$. In the time interval relevant for the WHFI the heat flux and (counter-)drifts are only partially relaxed, showing similar reductions of about 25% or 30% of initial magnitude. We can state that the relaxation of relative drift velocities, i.e., $U_{c,b}(t_{\rm max}) \approx 0.67 \ U_{c,b}(0)$, is slowed down by a concurrent effect of the enhanced fluctuations, which interact with the electrons and induce opposite temperature anisotropies in the core and beam populations.

In Figure 3 we plot the normalized power spectra for the initial stage of the simulation, i.e., $0 < \Omega_i t < 2.24$, to guarantee that we are capturing the linear stage of the WHF instability and have a fair comparison with the linear dispersion relation at $\Omega_i t = 0$. The spectra are obtained from $|FFT(B_v - iB_z)|^2$, where here the FFT is computed in space and time (then normalized to the maximum value of the spectra). By doing so, we are able to separate the contribution of left-hand (LH) and right-hand (RH) circularly polarized modes. Thus, for $\omega > 0$ we observe the RH contribution with positive and negative helicity, k > 0 and k < 0, respectively; see Saeed et al. (2017a) for details. Most of the magnetic power is concentrated in the part with $\omega > 0$ and k > 0, corresponding to the RH unstable modes with positive helicity, confirming the linear theory predictions (top panel) for an RH WHFI. Moreover, we observe a very low intensity in the

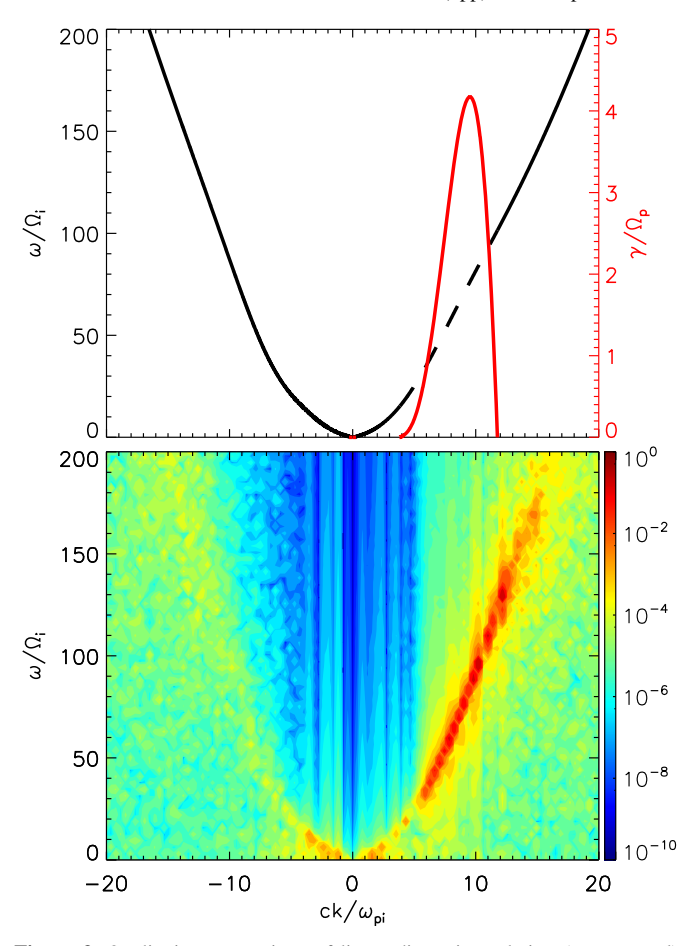


Figure 3. Qualitative comparison of linear dispersion relation (upper panel), real frequency (dashed black line representing the unstable region) and growth rate (red), with normalized power spectra of whistler fluctuations for the interval $0 < \omega_i t < 2.0$.

negative wavenumber part of the spectrum, but those are modes with negative helicity and are damped, according to linear calculations. The other combinations do not show any significant power (not shown here). Here we can state that our PIC simulations are capable of capturing the low-intensity whistler fluctuations associated with the WHFI that can develop only for $\omega > 0$ and k > 0. The dispersion shown by the simulated fluctuations is not an instantaneous picture, but rather a cumulative contribution of fluctuations in the entire period under consideration, when macroscopic plasma values evolve from the initial condition. However, the unstable wavenumber interval does not change much with the beaming speed (see Figures 1 and 2 in Shaaban et al. 2019) to explain the broad wavenumber spectra, which may probably result from the small error in the energy conservation in this simulation. Reducing the time step or increasing the number of particles per grid cell would help to improve the energy conservation and therefore obtain more accurate results, but more computational resources will be needed.

pdfelement

he velocity distribution function (VDF) evant stages of the simulation $\Omega_i t = 0.0$, total electron population (upper panels) at (lower panels), as well as the reduced along v_y) $f_e(v_x)$ at the initial and (almost)

mulation, i.e., $\Omega_i t = 0.0$, and 3.92 (right panel). In order to highlight the deformation of the electron components in the distribution, we have carefully selected three

particular contours, as indicated with dotted lines, at 2' 10⁻⁴, 3' 10⁻⁴, 8 10⁻⁴. It is clear that the highest contour of level 8×10^{-4} (dotted black line) becomes more symmetric at the end of the simulation, showing also a slight increase of temperature anisotropy of the core population $T_{c,^{\wedge}} > T_{c,}$ (upper panels) and giving an indication for the relaxation of the drift velocities. In the case of the beam (lower panels), this contour shows the behavior observed in Figure 1, a generation of parallel anisotropy. At later stages of the simulation contours of a lower level (white), e.g., 3×10^{-4} and 2×10^{-4} , are slightly different than those at the initial state, and specifically show an asymmetric skewness of lessscattered particles (pitch-angle scattering of the beam decreasing in parallel direction as electron energy increases). Moreover, a lower (relaxed) but still finite drift velocity is more obviously shown by the reduced distributions in the right panel. The reduced distributions confirm the previous description that the initial drift velocities (black line) are regulated by the enhanced WHFI fluctuations and the electron components ended up with small but finite relative drift velocities (blue line). Moreover, at the final stage, i.e., $\Omega_i t = 3.92$, the reduced electron velocity distribution function (eVDF) $f_e(v_x)$ shows the formation of a small, but still noticeable, "shoulder" in the parallel direction for the beam component, already suggesting that not all beaming electrons are scattered by the enhanced fluctuations, a hypothesis confirmed by the results in Figure 5.

Finally, Figure 5 shows the departures of the distributions from the initial condition $\delta f_i(t) = f_i(t) - f_i(0)$, for core (top panels) and beam (bottom panels) electrons, and for the two relevant moments $\Omega_i t = 2.24$ (left) and $\Omega_i t = 3.92$ (right). Red contours show $\delta f_i > 0$ with an abundance of scattered electrons, while blue contours $\delta f_i < 0$ mark the electron loss. Here we can see how different electron components are scattered (or not) by the whistler waves. Correlating with Figure 1, the diffusion of core electrons occurs due to the effect of whistlers that interact resonantly with the electrons with $v_x < |U_c|$, while the instability itself is (resonantly) triggered by the beaming electrons with $v_x < U_b$, cooling them down in perpendicular direction and increasing their effective temperature (or kinetic energy) in parallel direction. The lighter blue population at higher energies in the lower-right panel of Figure 5 indicates those electrons less scattered by whistlers, and corresponds to the small shoulder (or small plateau) shown in Figure 4. In time this population is naturally reduced leading to a lower pitch-angular width that becomes prominent due to a concomitant decrease of the drift.

3. Summary

In this Letter we have provided a detailed description of the WHFI using an implicit one-dimensional PIC simulation. The instability is triggered by the relative drift of the counterbeaming electron populations, without temperature gradients or temperature anisotropies. The initial stage of the simulation is characterized by a rapid growth of the magnetic energy density, corresponding to the excitation of the WHFI, then corroborated by the spectral analysis with a good agreement with linear theory. The enhanced whistler fluctuations interact with both electron components, reducing the relative drift ($\sim 30\%$) and inducing (effective) temperature anisotropies, i.e., an excess of perpendicular temperature for the core and excess of parallel temperature for the beam. The interplay of temperature anisotropies is in good agreement with a recent QL approach (Shaaban et al. 2019) (although the drift relaxation is less

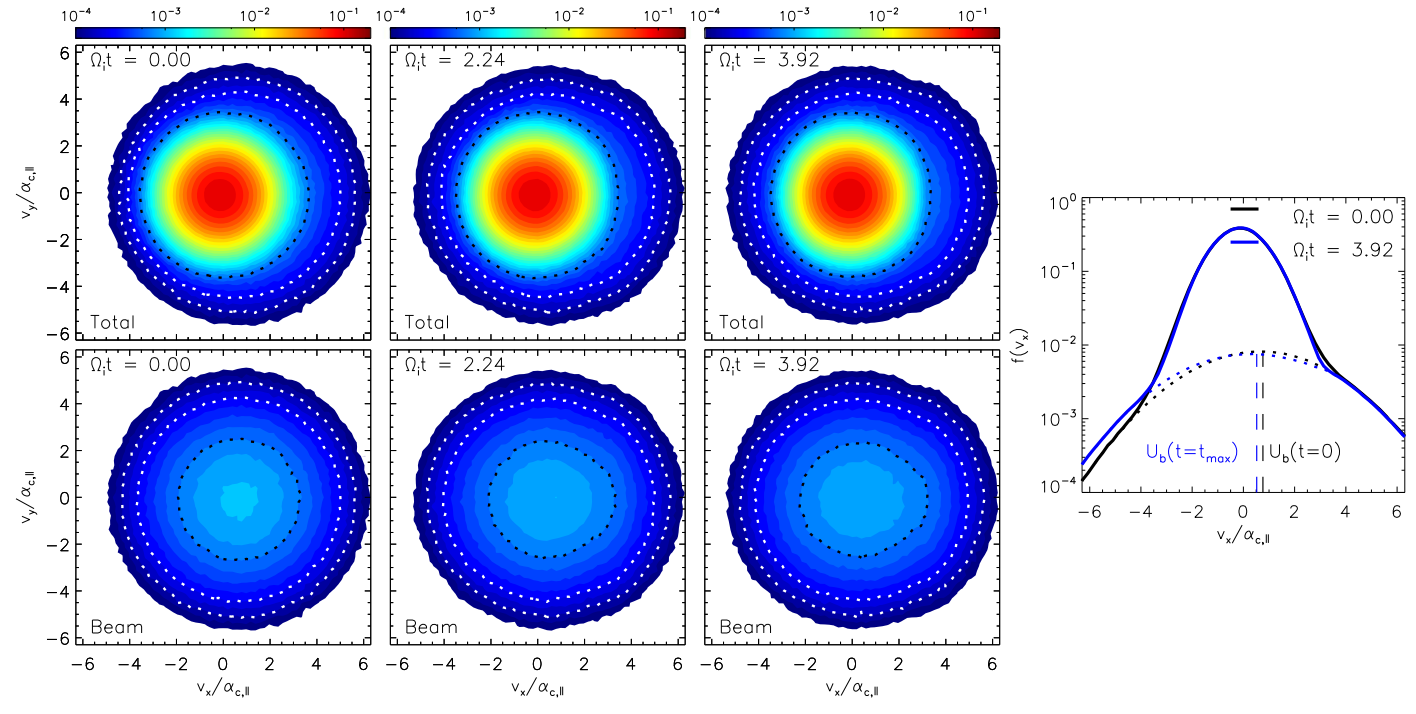


Figure 4. eVDF $f_e(v_x, v_y)$ at different stages in the simulation, $\Omega_i t = 0.0$ 3.3 and 10.1. The top panels show the total eVDF, and the bottom panels show only the beam distributions. Initial ($\Omega_i t = 0.0$; black) and final ($\Omega_i t = 10.1$; blue) snapshots of the reduced eVDF $f_e(v_x)$ (right panel).

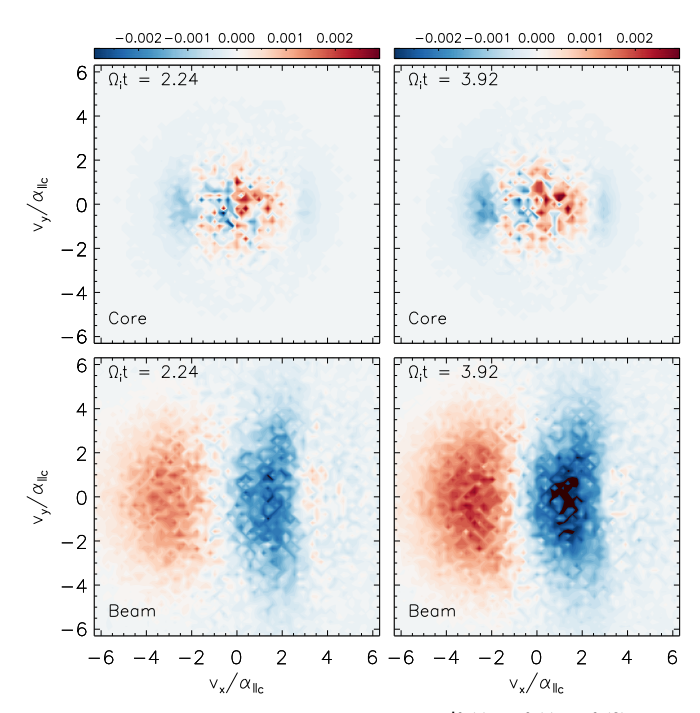


Figure 5. Fluctuating distribution function $df_j(t) = f_j(t) - f_j(0)$: core distribution δf_c (top row) and beam distribution δf_b (bottom row).

significant under the effect of a single mode in QL theory), and gely accepted belief that WHFI saturates litudes.

direction the strahl becomes skewed with tion decreasing in width as electron t seems to be characteristic of self-

generated winstiers and not to small-scale turbulence. However, this skewness (a decreasing pitch-angle distribution with increasing energy) is shown only by the lower levels (dashed white contours) with a lower contribution to the moments of the distribution, and implicitly to the effective temperature anisotropy, which is reduced.

Future refinements to clarify the nonlinear evolution of this instability need to be undertaken with caution and eventually new codes will need to be used that better conserve the energy.

These results were obtained in the framework of the projects SCHL 201/35-1 (DFG-German Research Foundation), GOA/2015-014 (KU Leuven), G0A2316N (FWO-Vlaanderen), and C 90347 (ESA Prodex 9). S.M.S. acknowledges support by a FWO Postdoctoral Fellowship, grant No. 12Z6218N. P.H.Y. acknowledges the BK21 Plus program from NRF Korea, NASA grant NNH18ZDA001N-HSR, and NSF grant 1842643 to the University of Maryland. The computational resources and services used in this work were provided by the VSC (Flemish Supercomputer Center), funded by the Research Foundation—Flanders (FWO) and the Flemish Government—department EWI. We acknowledge fruitful discussions at the meeting of international team on Kappa Distributions hosted by ISSI-Bern.

ORCID iDs

R. A. López https://orcid.org/0000-0003-3223-1498 S. M. Shaaban https://orcid.org/0000-0003-0465-598X

M. Lazar https://orcid.org/0000-0002-8508-5466

S. Poedts https://orcid.org/0000-0002-1743-0651

P. H. Yoon b https://orcid.org/0000-0001-8134-3790 A. Micera https://orcid.org/0000-0001-9293-174X

G. Lapenta https://orcid.org/0000-0002-3123-4024

References

Bale, S. D., Pulupa, M., Salem, C., Chen, C. H. K., & Quataert, E. 2013, ApJL, 769, L2

Berčič, L., Maksimović, M., Land i, S., & Matteini, L. 2019, MNRAS, 486, 3404

```
Breneman, A., Cattell, C., Schreiner, S., et al. 2010, JGRA, 115, A08104
Crooker, N. U., Larson, D. E., Kahler, S. W., Lamassa, S. M., & Spence, H. E.
   2003, GeoRL, 30, 1619
Gary, S. P. 1985, JGR, 90, 10815
Gary, S. P., & Feldman, W. C. 1977, JGR, 82, 1087
Gary, S. P., Neagu, E., Skoug, R. M., & Goldstein, B. E. 1999a, JGR, 104,
Gary, S. P., & Saito, S. 2007, GeoRL, 34, L14111
Gary, S. P., Skoug, R. M., & Daughton, W. 1999b, PhPl, 6, 2607
Gurgiolo, C., Goldstein, M. L., Viñas, A. F., & Fazakerley, A. N. 2012,
    nGeo, 30, 163
Horaites, K., Astfalk, P., Boldyrev, S., & Jenko, F. 2018, MNRAS, 480, 1499
Lacombe, C., Alexandrova, O., Matteini, L., et al. 2014, ApJ, 796, 5
Landi, S., Matteini, L., & Pantellini, F. 2014, ApJL, 790, L12
Lee, S.-Y., Lee, E., & Yoon, P. H. 2019, ApJ, 876, 117
López, R. A., & Yoon, P. H. 2018, JGRA, 123, 8924
Maksimovic, M., Zouganelis, I., Chaufray, J. Y., et al. 2005, JGRA, 110, 1
Markidis, S., Lapenta, G., & Uddin, R. 2010, Math. Comput. Simul, 80, 1509
Pagel, C., Gary, S. P., de Koning, C. A., Skoug, R. M., & Steinberg, J. T. 2007,
   JGRA, 112, A04103
Pavan, J., Viñas, A. F., Yoon, P. H., Ziebell, L. F., & Gaelzer, R. 2013, ApJL,
   769, L30
Pilipp, W. G., Miggenrieder, H., Mühlhäuser, K. H., et al. 1987, JGR, 92, 1103
Saeed, S., Sarfraz, M., Yoon, P. H., Lazar, M., & Qureshi, M. N. S. 2017a,
  MNRAS, 465, 1672
```

```
466, 4928
Saito, S., & Gary, S. P. 2007a, GeoRL, 34, L01102
Saito, S., & Gary, S. P. 2007b, JGRA, 112, A06116
Scime, E. E., Littleton, J. E., Gary, S. P., Skoug, R., & Lin, N. 2001, GeoRL,
Seough, J., Nariyuki, Y., Yoon, P. H., & Saito, S. 2015, ApJL, 811, L7
Shaaban, S. M., Lazar, M., & Poedts, S. 2018a, MNRAS, 480, 310
Shaaban, S. M., Lazar, M., Yoon, P. H., & Poedts, S. 2018b, PhPl, 25, 082105
Shaaban, S. M., Lazar, M., Yoon, P. H., Poedts, S., & López, R. A. 2019,
   MNRAS, 486, 4498
Spitzer, L., & Härm, R. 1953, PhRv, 89, 977
Stansby, D., Horbury, T. S., Chen, C. H. K., & Matteini, L. 2016, ApJL,
Tong, Y., Bale, S. D., Salem, C., & Pulupa, M. 2018, arXiv:1801.07694
Tong, Y., Vasko, I. Y., Artemyev, A. V., Bale, S. D., & Mozer, F. S. 2019a,
  ApJ, 878, 41
Tong, Y., Vasko, I. Y., Pulupa, M., et al. 2019b, ApJL, 870, L6
Vasko, I. Y., Krasnoselskikh, V., Tong, Y., et al. 2019, ApJL, 871, L29
Verscharen, D., Chandran, B. D. G., Jeong, S.-Y., et al. 2019a, arXiv:1906.
Verscharen, D., Klein, K. G., & Maruca, B. A. 2019b, arXiv:1902.03448
Vocks, C., & Mann, G. 2003, ApJ, 593, 1134
Vocks, C., Salem, C., Lin, R. P., & Mann, G. 2005, ApJ, 627, 540
Wilson, L. B., Koval, A., Szabo, A., et al. 2013, JGRA, 118, 5
```

Saeed, S., Yoon, P. H., Sarfraz, M., & Qureshi, M. N. S. 2017b, MNRAS,

